Correlation and Spectral Density Functions in Mode-Stirred Reverberation – III. Measurements

Luk R. Arnaut and John M. Ladbury

***Abstract*—Experimental auto- and cross-correlation functions of mode-stirred fields with corresponding spectral density functions are extracted from measured stir sweeps and compared with theoretical models derived in part I, using estimated spectral moments in part II. The second-order Padé approximant based model is confirmed to account for the main spectral features, including the slope near stir DC, corner frequency, level drop, and asymptotic spectral density at the Nyquist frequency. Ensemble averaging across secondary tune states yields spectral densities with reduced spectral bias and RMS fluctuation, compared to densities for individual stir sweeps or their concatenation. Periodogram- and correlation-based methods produce near-identical results. Distinctive theoretical features between power based vs. field based spectral densities are experimentally verified. Interchanging the roles of stirrer and tuner demonstrates the effect of stir efficiency on correlation and spectral density. The spectral characterization enables stirrer diagnostics to be performed, which is demonstrated through detection and identification of EMI by mains power harmonics in the measured stir spectrum.**

Keywords – EMI stirrer diagnostics, stir spectral density, stir spectrogram.

I. Introduction

In this part III article, measurement data obtained in a dual-paddle mechanically mode-stirred reverberation chamber (MSRC) as described in part II are used to extract empirical correlation functions (CFs) and spectral density functions (SDFs). The focus is on overmoded operation (CW operating frequencies $f \geq 2$ GHz in this MSRC), enabling a validation of theoretical results derived in parts I and II [1], [2].

Previously [3], power autocorrelation functions (ACFs) and SDFs in a mode-tuned chamber were obtained experimentally and modelled empirically, in a simplified way, based on scalar measurements using a power sensor and applying high-order exponential curve fitting. Nowadays, the availability of high-speed high-capacity vector spectrum or network analyzers (VSAs/VNAs) allows for extending that early work significantly, thereby no longer requiring the idealized assumption of complex circularity of the underlying received field $E(\tau)$ in [3], while also enabling I/Q cross-correlation functions (CCFs) and cross-spectral density functions (CSDFs) to be determined. In addition, the high sampling rate of VNAs provides insights into limitations of sampled sweeps for capturing the actual physical (i.e., time-continuous) field evolution, including stir noise data and its correlation properties.

A major motivation for modelling and validating ACFs and SDFs is to build a dynamic model of the stir process in support of a theory of mode stirring in continuous time (dynamic EM environment), i.e., beyond quasi-static mode tuning. As will be demonstrated in sec. VI-B, mode stirred operation enables certain EMI effects to be detected that would normally not be noticeable in typical mode-tuned operation exhibiting relatively large dwell times per state.

In this third part, theoretical expressions for the CFs and SDFs, for both fields and power as input quantities are compared and validated against results from experimental data to demonstrate the feasibility of the models and to intercompare their accuracy. The correlation structure is characterized by its calculable low-order spectral moments, as detailed in part II. All temporal and spectral processing is performed in "raw" format, i.e., without temporal nor spectral windowing for tapering of finite data sets, except for the inevitable truncation to one full stir period (paddle rotation) [2, sec. IV.A], in order to avoid biasing the mean and (co)variance.

The following notational conventions are adopted. m overdots indicate mth-order differentiation with respect to the dependent variable, being either the temporal continuous stir state τ or the stir frequency ϖ as its Fourier counterpart. Their sampled values are denoted by τ_n and ϖ_k, respectively. Single- and double-primed quantities refer to either the real (in-phase, I-) or imaginary (quadrature, Q-) part of the complex electric field $E = E' + \mathrm{j}E''$ with an assumed $\exp(\mathrm{j}\varpi\tau)$ stir dependence, or its complex correlation functions. We refer to 'auto' and 'cross' correlations or spectra as relating to the I- and Q-components of the complex E. Alternatively, one can obtain the complex autocorrelation of E with the complex conjugate of itself, E^*. For economy of notation, $E'^{(\prime)}$ denotes both E' and E'' as separate cases combined within a single expression, and similarly for $\lambda_i'^{(\prime)}$. As in part I, primed spectral moments $\lambda_i'^{(\prime)}$ already imply normalization by the field variance λ_0.

II. Experimental Set-Up

Details of the chamber, measurement configuration and instrumentation were given in [2, sec. V-A.]. The measurements reported here refer to a MSRC without absorber, but including an amplifier. Except in sec. VI-B, the 'large' short wide paddle is used in stirred mode (continuous rotation) while the 'small' tall slender paddle is used in tuned mode (stepped rotation). In sec. VI-B, the roles of both paddles are interchanged.

III. Correlation: ACF and CCF

A. ACF

For a wise-sense stationary (WSS) quasi-circular (QC) field $E(\tau) = E'(\tau) + \mathrm{j}E''(\tau)$ at lag for $\tau = t - t_0$, the ACF $\rho'_E(\tau)$

and CCF $\rho''_E(\tau)$ can be combined as

$$\rho_E(\tau) \equiv \rho'_E(\tau) + \mathrm{j}\rho''_E(\tau) = \langle E(0)E^*(\tau)\rangle/\sigma_E^2 \quad (1)$$

where $\sigma_E^2 = \sigma_{E'}^2 + \sigma_{E''}^2 \simeq 2\sigma_{E'^{(\prime)}}^2$ and

$$\rho'_E(\tau) \simeq \rho_{E'^{(\prime)}}(\tau) = \langle E'^{(\prime)}(0)E'^{(\prime)}(\tau)\rangle/\sigma_{E'^{(\prime)}}^2 \quad (2)$$

$$\rho''_E(\tau) \simeq -\rho_{E',E''}(\tau) = -\langle E'(0)E''(\tau)\rangle/(\sigma_{E'}\sigma_{E''}). \quad (3)$$

For N_s discrete data samples $\{E_n\}_{n=0}^{N_s-1}$ at $\tau_n = n\Delta\tau = t_n - t_0$, this requires the $N_s \times N_s$ covariance matrix $\underline{\underline{R}}_E$.

Alternatively, the ASDF can be calculated from the periodogram (i.e., directly from the Fourier transform $\mathcal{E}(\varpi)$ of the stir data $E(\tau)$), with which the EWK theorem can be applied to find the ACF from $\mathcal{E}(\varpi)$, without a need for constructing $\underline{\underline{R}}_E$, as [1, eq. (31)]

$$\begin{aligned} g_E(\varpi) &\equiv g'_E(\varpi) + \mathrm{j}g''_E(\varpi) = \langle \mathcal{E}(\varpi)\mathcal{E}^*(\varpi)\rangle \\ &= \langle [\mathcal{E}'(\varpi)]^2\rangle + \langle [\mathcal{E}''(\varpi)]^2\rangle + \mathrm{j}2\langle \mathcal{E}'(\varpi)\mathcal{E}''(\varpi)\rangle \end{aligned} \quad (4)$$

where $\mathcal{E}(\varpi) \triangleq \mathcal{F}[E(\tau)](\varpi)$ and $\mathcal{E}'^{(\prime)}(\varpi) \triangleq \mathcal{F}[E'^{(\prime)}(\tau)](\varpi)$, with $\langle \mathcal{E}'(\varpi)\mathcal{E}''(\varpi)\rangle \to 0$ for $N_s \to +\infty$. For N_s samples at times $\{\tau_n\}$ and N_s stir frequencies $\{\varpi_k\}$ $(n, k = 0, \ldots, N_s - 1)$, with the aid of an FFT algorithm, the periodogram is generally more efficiently computed than $\underline{\underline{R}}_E$ from the definition (2) when N_s is large. An efficient scheme for the computation of $\rho'_E(\tau)$ is therefore [1, eq. (32)]

$$\{E(\tau_n)\} \xrightarrow{\text{FFT}} \{\mathcal{E}(\varpi_k)\} \xrightarrow{(4)} \{g_E'^{(\prime)}(\varpi_k)\} \xrightarrow{\text{IFFT}} \{\rho_E'^{(\prime)}(\tau_n)\}. \quad (5)$$

Figs. 1(a) and (b) compare ACFs obtained using the definition- vs. periodogram-based methods, based on both $E(\tau)$ and $|E(\tau)|^2$ data at 2 GHz. The resulting ACF of E holds the middle between the ACFs of E' and E'', showing close correspondence with the IFFT of the periodogram for E. A similar level of agreement is found for the ACF of $|E|^2$ (black curve vs. green symbols). The plots in Fig. 1(a) also illustrate the theoretical relationship $\rho_{|E|^2}(\tau) \simeq [\rho_{E'^{(\prime)}}(\tau)]^2$ for ideal random fields.

An IFFT-based calculation produces the circular ACF, where data are presumed to originate from a periodic sequence with some period N_s. This represents the physical reality in an mechanically stirred ideal MSRC, where field values repeat exactly after one full rotation of the stirrer or tuner. To remove the circularity of the data and obtain agreement with the linear ACF, padding the data with N_s zeros prior to calculating the IFFT. Conversely, measuring data across multiple rotations and comparing their ACF from the definition with the circular ACF for one rotation offers a method for detecting departures from ideal periodicity and slow[1] mechanical drift. Fig. 1(b)(iii) shows the residuals between definition- and zero-padded IFFT-based ACFs $\rho'_E(\tau)$ at $f = 2$ GHz, indicating that the extent of correlation circularity is maximally of the order of ~ 0.05, decreasing to ~ 0.03 at $f = 18$ GHz, thus offering a target for ACF approximation accuracy in practice and indicating a $[1 - (\Delta\tau/N_s)]^{-1}$ dependence, on average. Corresponding residuals for the CCF are show in Fig. 2(b)(ii).

[1]For investigation of nonstationarity within one period (fast drift or fast fading), local methods of analysis are required, e.g., using wavelets.

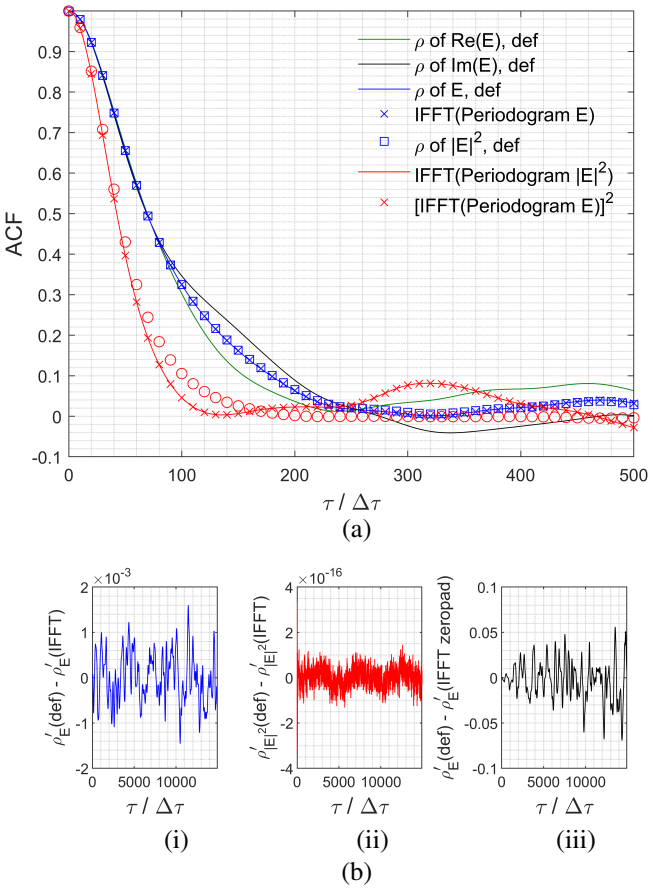

Fig. 1: (a) Definition- vs. periodogram-based ACF, (b) (i)-(ii) their discrepancy between definition and circular IFFT calculation, and (b)(iii) between definition-based and zero-padded IFFT, for $E'^{(\prime)}$, E and $|E|^2$, at $f = 2$ GHz.

B. CCF

For quasi-circular random fields with no deterministic component, the CCF $\rho''_E(\tau) \simeq [\rho_{E'',E'}(\tau) - \rho_{E',E''}(\tau)]/2 \simeq \rho_{E'',E'}(\tau)$ vanishes at $\tau = 0$, i.e., simultaneous $E'(\tau)$ and $E''(\tau)$ are uncorrelated. Since a CCF measures the linear cross-dependence as a function of lag τ, it evaluates the phase shift between I- and field Q-components in the received field, which can be used for extracting unstirred or line-of-sight components. A nonzero cross-correlation at some τ determines an average level of I/Q correlation, indicating a mean modulation in communications, i.e., mutual information content.

A second application is the detection of the stir period in a stir sweep that extends beyond a single full turn of the mode stirrer: by cross-correlating sweep data in a window of length N with data in a stepwise sliding window of the same length yields the start of the next period at the location where ths cross-correlation shows a maximum (peak) value. This technique is robust to small levels of noise and drift.

Fig. 3 compares ACFs and CCFs at $f = 2$ GHz for assumed

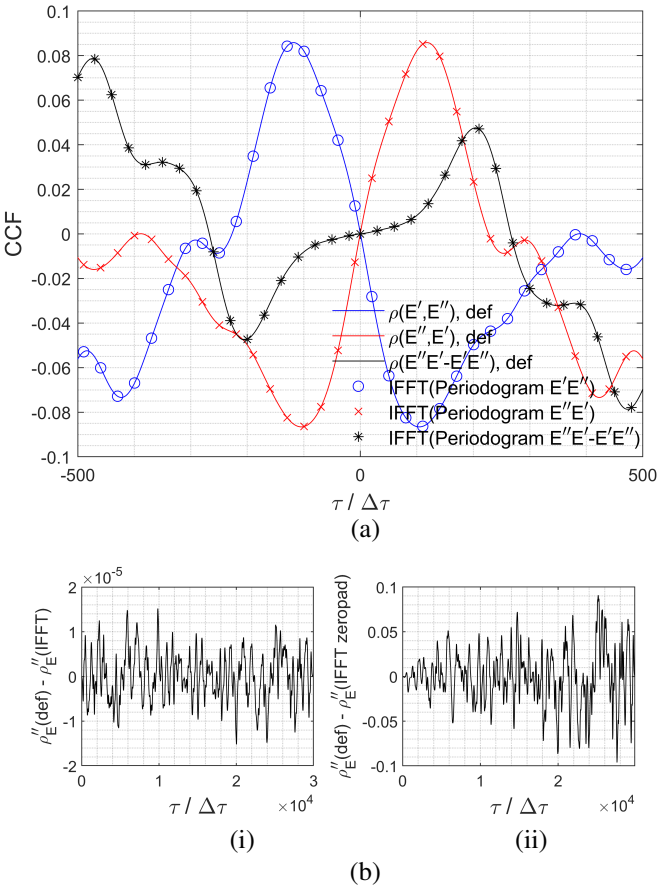

Fig. 2: (a) Definition-based vs. periodogram-based (without zeropadding) CCF for E', E'', and E. (b) Difference between definition-based and IFFT-based CCF (i) without and (ii) with zero-padding of E, at $f = 2$ GHz.

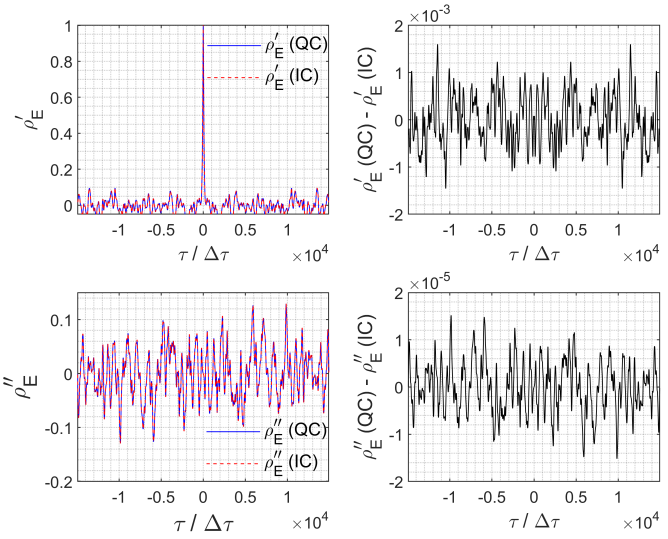

Fig. 3: ACF (top left) and CCF (bottom left) of complex E at $f = 2$ GHz, tuner state 1 of 72: comparison between ideal circularity (IC) and actual quasi-circular approximation (QC), with respective residuals for ACF (top right) and CCF (bottom right).

ideal circular (IC) fields, i.e.,

$$\rho_E^{(\mathrm{IC})}(\tau) = \frac{\sigma_{E',E'}(0,\tau) + \sigma_{E'',E''}(0,\tau)}{\sigma^2_{E'}(0) + \sigma^2_{E''}(\tau)} \tag{6}$$

which reduces for quasi-circular (QC) uniform fields to

$$\rho_E^{(\mathrm{QC})}(\tau) \simeq \frac{1}{2}\left\{\left[\rho'_{E',E'}(0,\tau) + \rho'_{E'',E''}(0,\tau)\right] + \mathrm{j}\left[\rho''_{E'',E'}(0,\tau) - \rho''_{E',E''}(0,\tau)\right]\right\}. \tag{7}$$

The plots indicate that ideal circularity is closely approximated for these data, with deviations being of the order of just 1% for $\rho'_E(\tau)$ and 0.01% for $\rho''_E(\tau)$.

C. Padé vs. Taylor Approximation Models for CFs

Fig. 4(a) compares first- and higher-order Taylor and Padé approximations to the actual (i.e., sample) reference ACF at $f = 18$ GHz. The ACF $\rho_{E,E^*}(\tau)$ is midway between $\rho_{E',E'}(\tau)$ and $\rho_{E'',E''}(\tau)$, as expected for quasi-circular $E(\tau)$. The $[0/2]$-order Padé approximation in τ^2 closely tracks the experimental sample ACF over a wide domain of τ-values, significantly outperforming the Taylor expansions in τ^2. Even a Padé approximation of first-order $[0/1]$ in τ^2 already offers a superior match across a wider domain compared to a third-order Taylor expansion. Specifically, the correlation length associated with the 1/e-level of the experimental ACF is seen to be approximately $\tau/\Delta\tau \simeq 10$, serving as a reference value. In comparison, second- and third-order Taylor approximations exhibit a close match up to merely three lag units and correlation level 0.7. By contrast, first- and second-order Padé approximants offer a close match up to 15 and 25 lag units and down to levels of 0.2 and 0.1, respectively. Larger τ-domains for close correspondence are expected at lower frequencies, but are also found for less efficient stirring, as demonstrated in sec. VI-B.

Fig. 4(b) shows first- and higher-order approximations to the actual sample CCF. The deviation from linearity of $\rho''_E(\tau/\Delta\tau)$ is seen to set in rapidly, after just a few units, indicating asymmetry of the amplitude spectrum and nonlinearity of the process from this point onward. Compared to the ACF, the Padé approximations still offer an improved fit compared to Taylor expansions, although now more rapidly departing from the experimental CCF outside the region of convergence (cross-correlation length), yet still offering an improved fit, even for a reduced order of Padé approximation. Crucially, and unlike Taylor expansions of any order, the Padé approximants also exhibit a correct asymptotic dependence for $|\tau| \to +\infty$ in both the ACF and CCF.

In summary, the domain where a good fit for CFs can be achieved is considerably larger for a Padé approximation than for a Taylor expansion, for equal orders of approximation and beyond. Inevitably, this domain is still restricted because both types of expansions are point-wise with reference to $\tau = 0$. For the purpose of approximating $\rho'^{(\prime)}_E(|\tau| \leq \tau'^{(\prime)}_c)$ for practical EMC/EMI applications [3], [4], this is sufficient because their drop of ACF level at τ'_c is well below 1/e. Beyond this domain,

other methods for modelling CFs can be adopted, e.g., using interpolating functions.

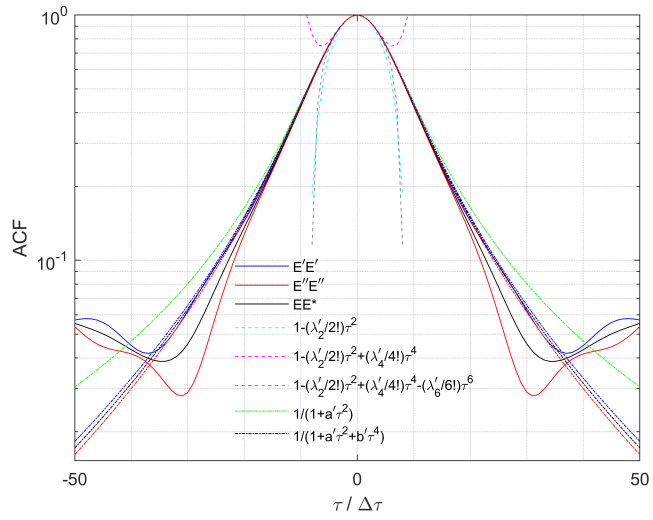

(a)

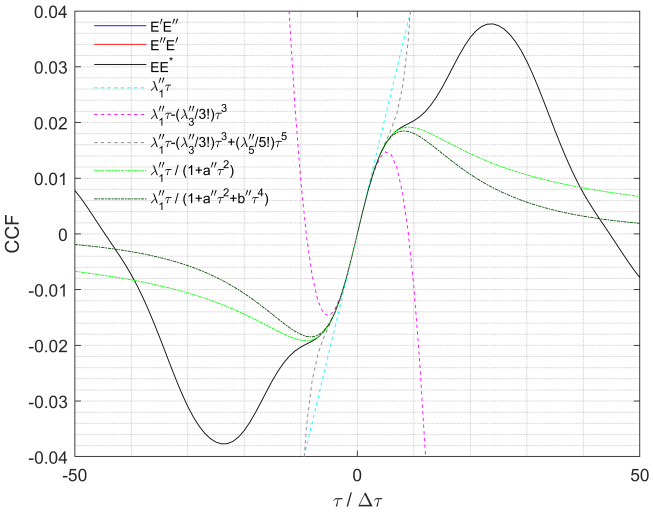

(b)

Fig. 4: (a) I/I and Q/Q ACFs for E', E'', E, and (b) I/Q and Q/I CCFs for E (solid), compared with 1st-, 2nd-, and 3rd-order Taylor (dashed), 1st-order Padé (green dot-dashed; for E) and 2nd-order Padé (other dot-dashed using the same color coding as for the experimental ACFs; for E', E'', E) approximations, at $f = 18$ GHz.

IV. Field Spectral Densities

A. ASDF

1) Spectrum: Since no spectral windowing is applied, the ASDF coincides with the periodogram of the data. Fig. 5 compares the ASDF of E for measured data at $f = 18$ GHz, based on application of the EWK theorem (i.e., FFT of the sample ACF matrix i.e., constructed from $E(\tau)$) vs. periodogram (squared amplitude of FFT of complex $E(\tau)$), against first-order (ideal negative exponential) and second-order SDF models for $g'_E(\varpi)$ and its envelope, as given by eqs. (37) and (38) in part I, showing good agreement. The first-order Padé-based ASDF is seen to accurately estimate the mean level and rate of low-frequency (LF) decay in the experimental $g'_E(\varpi)$; the second-order model offers the advantage of additionally estimating the stir high-frequency (HF) asymptotic level.

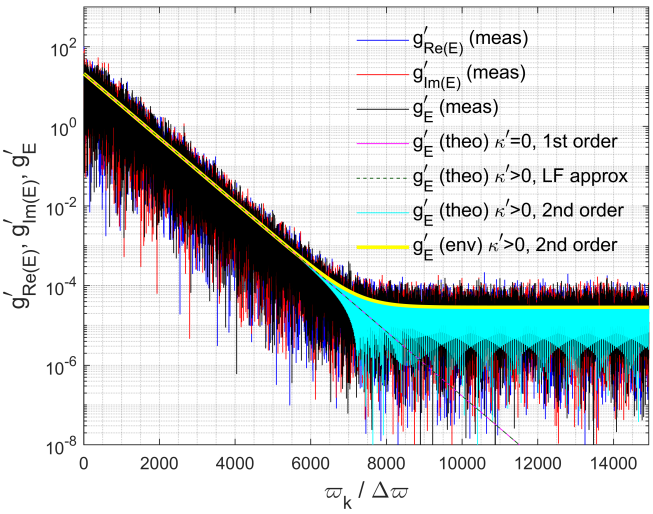

Fig. 5: Comparison of experimental vs. theoretical ASDFs $g'_E(\varpi_k/\Delta\varpi)$: 1-st-order exponential ($\kappa' = 0$), LF-approximating and general 2nd-order Padé-based models ($\kappa' = 5 \times 10^{-13}$), and envelope of ASDF as a function of $k = \varpi_k/\Delta\varpi$ for $0 \le k < N_s/2$ and $\Delta\varpi = 2\pi/N_s$.

Fig. 6 compares normalized ASDFs for wide short paddle stirring, obtained as periodograms in three different ways: (i) from a single stir sweep, at an arbitrary angular state of the small second paddle, yielding $N_s = 29\,869$ stir frequencies; (ii) from the "super" stir sweep constructed by concatenating all 72 tuned sweeps, i.e., for all 72 angular states of the small paddle ($N = N_t N_s = 72 \times 29\,869$); (iii) as an ensemble averaged ASDF, from all 72 individual ASDFs ($N_s = 29\,869$ stir frequencies), averaged for each ϖ_k. For (ii) and (iii), each individual ith sweep is weighted by its variance $\lambda_{0,i}$ prior to aggregation ($i = 0, \ldots, 71$). Concatenation – and, more generally, increasing N_s in a single stir sweep – increases spectral resolution within the ASDF, but does not decrease the range of mean square fluctuations, although it decreases the covariances $\langle \mathcal{E}'^{(\prime)}(\varpi_1)\mathcal{E}'^{(\prime)}(\varpi_2)\rangle$, on average, for an arbitrary pair (ϖ_1, ϖ_2) [5].

Fig. 6 (bottom) shows the average ASDF $\langle g'_E(\varpi)\rangle$. Its value at stir DC is zero because, in this analysis and unlike in [3], field data were centered (removal of any unstirred field [2]) prior to processing. The average ASDF reaches a maximum just in excess of $\varpi \simeq 0.001$, decays rapidly until $\varpi \simeq 0.01$, stays approximately constant until $\varpi \simeq 0.1$, before decaying exponentially until about $\varpi_{\max} = \pi/2$. A flattening of $\langle g'_E(\varpi)\rangle$ at LFs occurs for $0.002 < \varpi/\pi < 0.02$, caused in part by the finite window length. For $\varpi \to 0+$, the slope of $\langle g'_E(\varpi)\rangle$ approaches zero. Since a leading quadratic dependence of $\langle g'_E(\varpi)\rangle$ near $\varpi = 0+$ implies a finite second-

Parameter	[0/2] Padé	[0/2] Padé, set value κ'	measured
$(\lambda_2')^{1/2}$ (rad/s)	595.6	595.6	
$(\lambda_4')^{1/4}$ (rad/s)	926.3	932.1644	
FD debiased κ'	0.01118	5×10^{-13}	
$g_E'(\pi)/g_E'(0+)$ (dB)	-9.7	-61.5	-60.1
ϖ_c' (rad)	1.22	1.25	1.51
$\dot{g}_E'(\varpi \ll \varpi_c')$ (dB/rad)	-52.3	-52.5	-43.0

TABLE I: ASDF DC-to-Nyquist level drop $g_E'(\pi)/g_E'(0+)$, normalized corner frequency ϖ_c', and LF slope $\dot{g}_E'(\varpi \ll \varpi_c')$ for $g_E'(\varpi_k)$ averaged across 72 tuner states, at $f = 18$ GHz: measured results and [0/2] Padé-based ASDF results for finite-difference (FD) debiased value $\kappa' = 0.01118$ vs. ad hoc value $\kappa' \triangleq 5 \times 10^{-13}$.

order correlation moment i.e.,

$$\theta_2' \triangleq \int_{-\infty}^{+\infty} \tau^2 \rho_E'(\tau) \mathrm{d}\tau < +\infty \tag{8}$$

this suggests a higher-order approximant of the ACF for potential further model refinement (faster decay for $|\tau/\tau_c'| \gg 1$).

In part I, several theoretical HF asymptotic values for the continuous ASDF for the $[0/2]$ Padé approximant were derived. Tbl. I compares their predicted values with those for the measured data. It is seen that, as predicted, the DC-to-Nyquist level drop is highly sensitive to the value of κ', whose value is difficult to estimate accurately from sampled data, even after compensation for finite-difference bias (cf., part II). If, instead, a value of κ' is assigned and λ_4' is increased accordingly – in this case by 0.65% – while keeping λ_2' fixed, closer agreement can be found. Inclusion of further higher-order Padé approximant terms and/or increase of f may lead to further improved agreement between theoretically predicted and measured spectral characteristics.

2) Stir Spectral Coefficient of Variation: The ensemble of stir SDFs generated by varying the tune states of the secondary paddle, τ_2, allows for constructing a 2-D stir spectrogram, considered as a random function with stir sweeps as realizations (sample functions). A simpler 1-D summary representation is afforded by a summary statistic of the SDF, e.g., $\langle g_E'(\varpi_k)\rangle$ and $\sigma_{g_E'}(\varpi_k)$ across 72 tune realizations, at arbitrary ϖ_k. Fig. 7 shows the coefficient of variation, $\nu_{g_E'}(\varpi_k) = \sigma_{g_E'}(\varpi_k)/\langle g_E'(\varpi_k)\rangle$. At $f = 18$ GHz and $\varpi_k > 0$, its values fluctuate uniformly around the value one, corresponding to χ_2^2-distributed $|\mathcal{E}(\varpi_k > 0; \tau_2)|^2$ while $|\mathcal{E}(\varpi_k = 0; \tau_2)|^2$ are χ_1^2-distributed [6]. Therefore, regardless of $\Delta\tau$ in the primary stir sweep, the 72 samples $\mathcal{E}(\varpi_k; \tau_{2,\ell})$ for arbitrary ϖ_k follow a (quasi-)circular Gaussian distribution. At lower f, the $\nu_{g_E'}(\varpi_k)$ remain centered around one only for sufficiently low $\varpi_k > 0$, i.e., for large sample separations. Upward from some f-dependent transition frequency ϖ_o, the $\nu_{g_E'}(\varpi_k)$ increase sharply, as the corresponding stir arcs are too small to provide good stir statistics. This ϖ_o decreases with decreasing f, as the stir arc traversed during a given τ_n becomes progressively shorter relative to the CW wavelength. A more detailed analysis shows that the jump of $\nu_{g_E'}$ at ϖ_o corresponds to the transition in $g_E'(\varpi)$ from an exponential decay to flat correlation noise. For example, at $f = 4$ GHz, the jump in $\nu_{g_E'}(\varpi_k)$ occurs at $\varpi_o \simeq \pi/6$ rad, corresponding to $\varpi_o/\Delta\varpi \simeq 2490$.

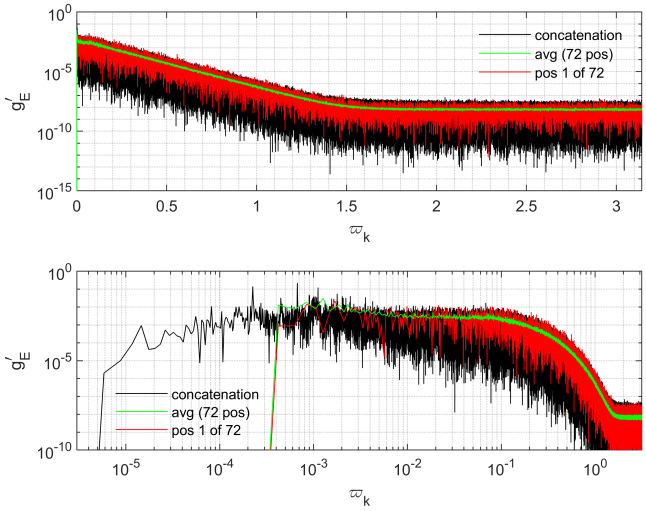

Fig. 6: Field ASDFs $g_E'(\varpi_k)$ calculated as periodograms, based in stir sweeps at 72 small paddle tune states (tuner step size 5 deg): (i) single sweep at one state with $N_s = 29\,869$ (red), (ii) averaged ASDFs across 72 states with $N_s = 29\,869$ (green), (iii) concatenation of 72 states with $N_s = 72 \times 29\,869$ (black), as a function of max-normalized stir frequency $\varpi_k = k\Delta\varpi = 2k\pi/N_s$ with $\varpi_{\max} = \varpi_{N_s/2} = \pi$ rad. Top: linear stir frequency scale, bottom: logarithmic stir frequency scale.

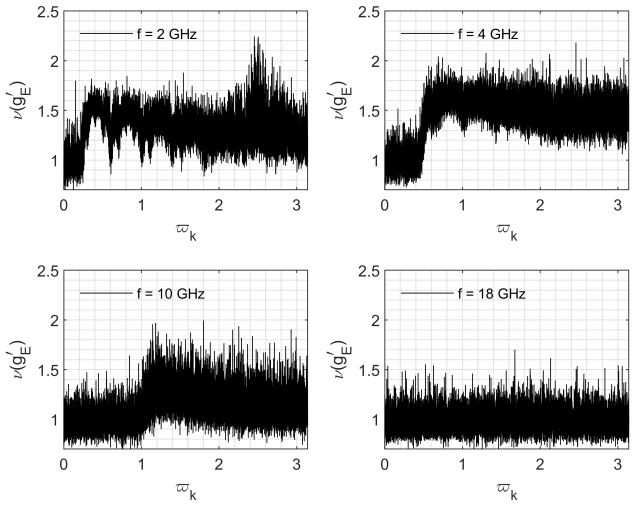

Fig. 7: Stir spectral coefficient of variation $\nu_{g_E'}(\varpi_k)$ associated with average ASDF at $f = 2$, 4, 10, and 18 GHz.

B. CSDF

The CSDF $g_E''(\varpi)$ represents the spread of the I/Q covariance $\sigma_{E',E''}$ across the spectrum of stir frequencies. It indicates whether a particular stir frequency contributes comparatively more or less to $\sigma_{E',E''}(0,\tau)$. Fig. 8 compares envelopes

of zeroth-, first-, and second-order Padé-based CSDF models for $g''_E(\varpi_k/\Delta\varpi)$ with EWK-based[2] CSDFs obtained from the experimental CCF, at $f = 18$ GHz. The theoretical CSDF envelopes are derived from eqs. (55), (57) and (64) in part I and from estimated λ''_i values corrected for finite-differencing bias (cf. part II). Increasing the Padé order is seen to yield improved agreement of both LF and HF asymptotic regimes of the CSDF, on average. Such improvement by increasing the order may also be expected for the LF part of the ASDF.

Comparing Fig. 8 for $g''_E(\varpi_k/\Delta\varpi)$ with Fig. 5 for $g'_E(\varpi_k/\Delta\varpi)$ shows that the latter achieves a better fit. This is commensurate with general properties of discrete Fourier sine and cosine transformations, respectively, as the latter typically produces a more efficient and accurate spectral representation, for arbitrary orders, compared to the former.

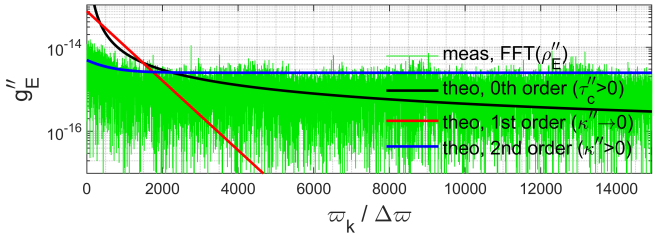

Fig. 8: Measured CSDF (EWK method) vs. theoretical 0th-, 1st-, and 2nd-order Padé-based CSDF envelopes of $g''_E(\varpi_k/\Delta\varpi)$ for $\tau''_c = 5\Delta\tau = 1.328$ ms, $\kappa'' \to 0$, and $\kappa'' = 0.0854$, respectively, at $f = 18$ GHz for stirring by wide short paddle.

Fig. 9 compares LF relative levels and decay rates of ASDF vs. CSDF. At $f = 18$ GHz, the rate of the exponential decay of the CSDF, $\sqrt{\lambda''_3/(6\lambda''_1)} = 412.8$ rad/s, is close to the rate for the ASDF, $\sqrt{\lambda'_2/2} = 421.1$ rad/s. This is no coincidence, as both rates arise as ratios of the first two Taylor expansion terms for $\rho''_E(\tau)$ and $\rho'_E(\tau)$, respectively. Their close numerical values underline the fact that expanding both the ACF and CCF to the same order results in similar levels of accuracy. Consequently, the ratios in Fig. 9(c) and (d) across tune states and CW frequency are typically of order 1.

V. Power Spectral Density

As indicated earlier, the practical measurement of spectra may rely on using a simpler scalar analyzers, e.g., EMI receivers or power meters. Such instruments cannot resolve the I- and Q-components individually, so that an assumption about their statistical mutual relationship must be made, e.g., ideal circularity. Then, the energy or power, proportional to the intensity $|E|^2$, becomes the input quantity for extracting the SDFs, here referred to as the power SDF (PSDF).

Fig. 10 compares the measured PSDF of $|E|^2$, $g'_U(\varpi)$, based on the EWK theorem (i.e., FFT of covariance-based ACF of $|E|^2$) vs. the periodogram-based ASDF (i.e., squared amplitude of the FFT of $|E|^2$), including a comparison to an ideal exponential ASDF for E (or 0th-order PSDF). The

[2]CSDFs obtained using the I/Q periodograms (not shown) were found to be nearly identical.

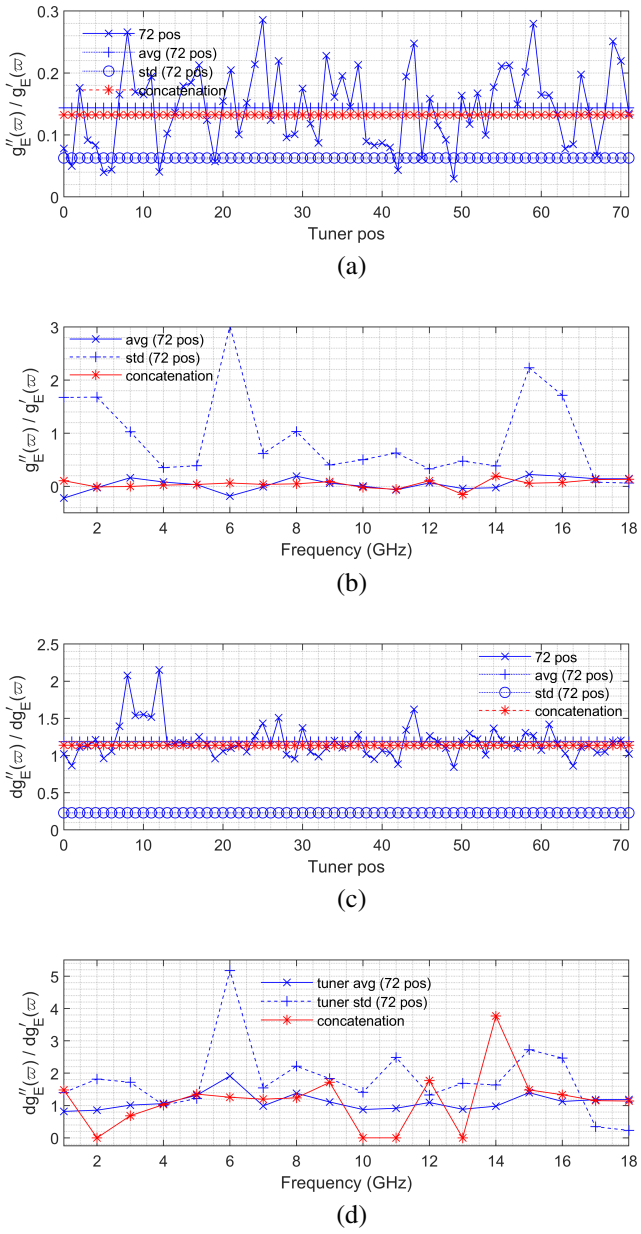

Fig. 9: (a) CSDF-to-ASDF level ratio $g''_E(\varpi)/g'_E(\varpi) = 6\sqrt{2\lambda'_2}(\lambda''_1)^2/\lambda''_3$ for $f = 18$ GHz at low ϖ (average 0.144; standard deviation 0.063); (b) tuner averaged mean and standard deviation of $g''_E(\varpi)/g'_E(\varpi)$ as a function of f, compared with values for concatenated sweep. (c) CSDF-to-ASDF slope ratio $\dot{g}''_E(\varpi)/\dot{g}'_E(\varpi) = \sqrt{3\lambda'_1\lambda'_2/\lambda'_3}$ at $f = 18$ GHz (average 1.186; standard deviation 0.230); (d) tuner averaged mean and standard deviation of $\dot{g}''_E(\varpi)/\dot{g}'_E(\varpi) = \sqrt{3\lambda'_1\lambda'_2/\lambda'_3}$ as a function of f, compared with values for concatenated sweep.

results validate the models in [1, sec. V] and [3]. Since the input $|E|^2$ is real-valued, $g''_U(\varpi) = 0$ hence $g_U(\varpi) \equiv g'_U(\varpi)$.

VI. ASDF and PSDF at Different CW Frequencies

A. Efficient Stirring

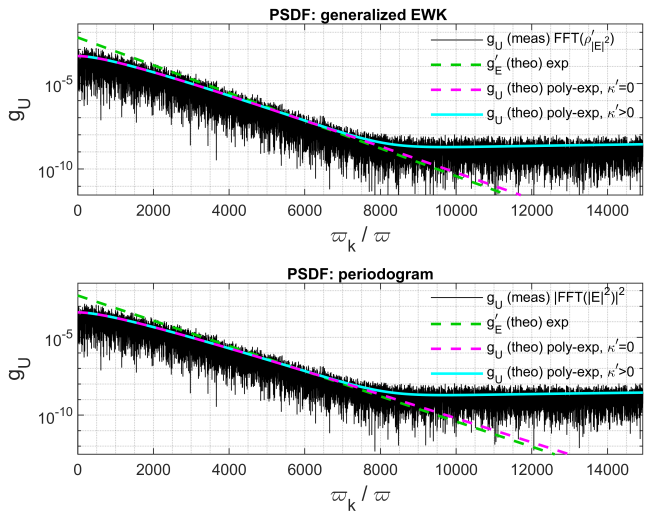

Fig. 10: Experimental PSDF $g_U(\varpi)$ (black) vs. generalized EWK theorem (top) or periodogram (bottom), compared with theoretical exponential zeroth-order (green), polynomial-exponential first-order (magenta) and second-order (cyan) Padé approximant based models.

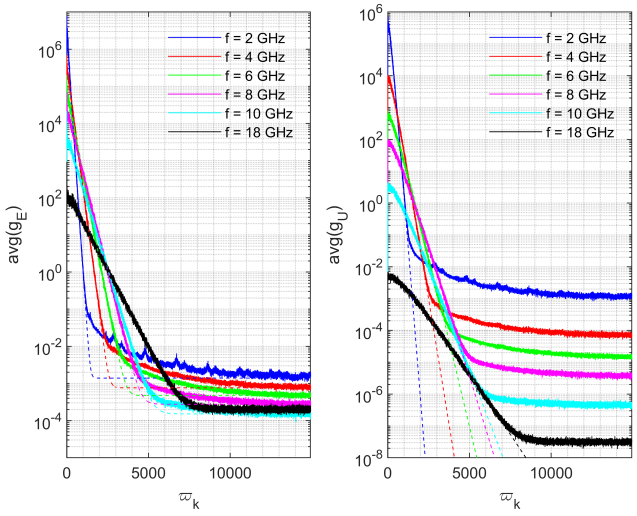

(a) (b)

Fig. 11: Comparison of (a) ASDFs and (b) PSDFs as functions of ϖ_k (in units $\Delta\varpi$): Padé-based models (dashed) vs. 72-sweep average of measured SDFs (solid) at selected CW frequencies f, for stirring of large paddle and averaged tuning of small paddle.

Fig. 11 compares the tuner averaged ASDFs (for E) and PSDFs[3] (for $|E|^2$) with the Padé models developed in part I, also showing LF and HF asymptotic approximations (dashed) based on the values of the spectral moments extracted from the data (cf. part II). Good agreement is found for the stir DC and Nyquist asymptotic dependencies and levels of the average g'_E). Fig. 11(a) indicates that the increase of κ' with decreasing f is primarily caused by the increasing stir DC level, and less because of the decreasing Nyquist level. For lower f, an extension to include higher-order ($m > 2$) Padé approximants involving additional deviation parameters $\kappa'^{(\prime)}_m$ [1, eqs. (38) and (67)] allows for further refinements to the estimated corner frequency, asymptotic slopes, and levels.

The changing profile of $g'_E(\varpi)$ with decreasing f in Fig. 11 originates from the similarity property of Fourier transforms,

$$\mathcal{F}\left[\rho'^{(\prime)}_E(\tau/\tau'^{(\prime)}_c)\right](\varpi) = \tau'^{(\prime)}_c g'^{(\prime)}_E(\tau'^{(\prime)}_c\varpi) \tag{9}$$

in which the correlation length $\tau'^{(\prime)}_c$ provides a scaling parameter. In particular, if f increases then $\tau'^{(\prime)}_c$ decreases, causing a contraction of $\rho'^{(\prime)}_E(\tau/\tau'^{(\prime)}_c)$ around $\tau = 0$ for $\tau'^{(\prime)}_c > \Delta\tau$. In accordance with (9), $g'^{(\prime)}_E(\varpi)$ then stretches (dilation of stir frequency) and flattens (lowering of spectral amplitudes) as the SDF evolves towards ideal white stir noise when $f \to +\infty$.

For the nth derivative of the CF,

$$\mathcal{F}\left[\rho'^{(\prime)(n)}_E(\tau)\right](\varpi) = (-\mathrm{j}\varpi)^n g'^{(\prime)}_E(\varpi). \tag{10}$$

In particular, $|\dot{\rho}_{E'^{(\prime)}}(|\tau| \to 0)| = \varpi g_{E'^{(\prime)}}(\varpi)$ for $\varpi \to \varpi_{\max}$, signifying that the rate of CF decay at small lags relates to the asymptotic HF part of the SDF, ideally $g_{E'^{(\prime)}}(\varpi_{\max} \to +\infty) \to 0$ when $\tau \to 0$ for mean-square differentiable $E(\tau)$.

B. Stirrer Diagnostics Based on ASDF

Dual-stirred chambers have been investigated before (cf., [7] and references therein) to compare synchronized vs. interleaved tuning, using both paddles in conjunction. Here, we use interleaved stirring to compare the performance of the individual paddles within the *same* chamber. This eliminates the effect of the enclosure itself (geometry, volume). In effect, it provides a substitution method for stirrers.

Fig. 12 shows SDFs obtained after interchanging the roles of stirrer and tuner, i.e., now for mode stirring (spinning) by the tall narrow paddle and mode tuning (stepping, with a view to ensemble averaging) by the short wide paddle. A comparison with Fig. 11 indicates a now reduced stir efficiency, manifested by the steeper slope of the SDFs at low ϖ (reduced $\sqrt{\lambda'_2}$; cf. eq. (42) in part I) and a lower corner frequency ϖ'_c, at all CW frequencies but *a fortiori* at larger f. Correspondingly, in Fig. 15, an increased correlation length $\tau'^{(\prime)}_c$ is witnessed, compared to Fig. 4. Note also that stirrer size and excitation frequency are not fully interchangeable in terms of stir efficiency, as can be witnessed, from the sharper corner transition for $f = 18$ GHz in Fig. 12 compared to that for $f = 2$ GHz in Fig. 11.

Earlier experimental [8] and theoretical [9] findings have indicated that wider paddles – i.e., with a larger diameter of their swept volume – exhibit greater stirring efficiency than narrower paddles. However, the present results cannot be used to confirm those findings because of the large difference in the swept volume of both paddles here (sec. II).

Periodic spikes are prominent in the SDFs of the stirred small paddle in Figs. 12 and 14(b), especially at lower f, while being more subdued for stirring by the large paddle

[3] In Fig. 11(b), the average PSDFs have not been normalized in order to separate and show the individual curves for different f more clearly.

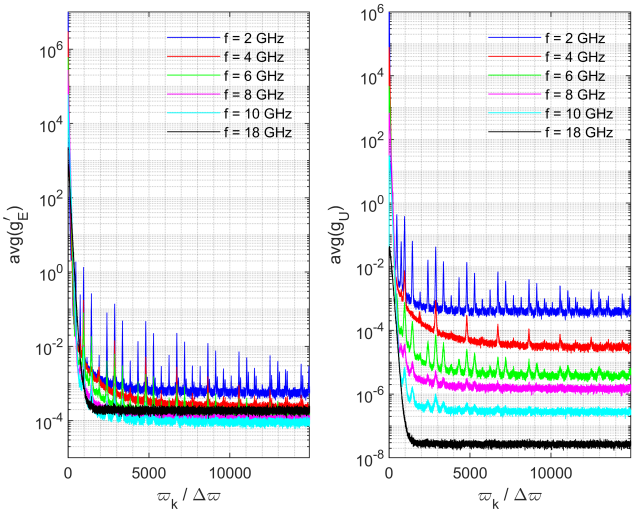

Fig. 12: Same as Fig. 11 but for interchanged roles of small and large paddles, now as stirrer and secondary tuner, respectively.

in Figs. 11 and 13(b) for the small paddle. The spikes increase λ_4' and hence κ'. In Figs. 12(a) and 14(b), strong peaks occur at all integer multiples of $\Delta k = 480 \pm 1$. These represent quasi-harmonics of a fundamental centered at $f_{\rm EMI} = (480 \pm 1)\Delta\varpi/(2\pi) \simeq 60.50 \pm 0.13$ Hz, i.e., traceable to EMI by unfiltered mains power. Additional weaker LF sub- and interharmonics are observed at $k \equiv \varpi_k/\Delta\varpi \simeq 121$, 235, 750 and 1172, which may have a small bias as they sit on the negative slope of the average SDF. Further HF interharmonics occur at $k_n \simeq 480n + 100$. ***On a logarithmic frequency scale as in Fig. 6 and from Fig. 14(a), a weak LF component and harmonics for $f \sim 7 \ldots 8.5$ Hz can be gleaned.***

In general, by considering the minimum and maximum detectable spacings in the frequency comb of a sampled harmonic EMI signal, viz., $2 \le \Delta k \le \lfloor N_s/2 \rfloor$, the range of unambiguously detectable EMI harmonics follows as

$$\Delta\varpi/\pi \le f_{\rm EMI} \le \lfloor N_s/4 \rfloor \Delta\varpi/\pi \qquad (11)$$

i.e., $2/T_s \le f_{\rm EMI} \le (2\Delta\tau)^{-1}$, here 0.252 Hz $\le f_{\rm EMI} \le 1882$ Hz. The upper bound in (11) can be increased by several orders of magnitude when using a state-of-the-art VSA instead [4].

The stir spectrogram in Fig. 14(c) reveals weak inhomogeneity through secondary tuning by the large paddle, e.g., at $\ell \equiv \tau_{2,\ell}/\Delta\tau_2 = 17$ where $g_E'(\varpi_k/\Delta\varpi)$ exhibits a larger value of κ' (cf. [1, Fig. 1]; less efficient stirring), apparent from a lighter horizontal band, while more efficient stirring occurs, e.g., at $\ell = 60$, represented by a darker band. The vertical stripe pattern indicates that the EMI in this experiment is non-intermittent, existing at the same frequencies throughout the stirring and tuning processes, and that the tuning performance is roughly uniform. Also the line widths differ. More generally, the stir spectrogram can be used for detecting intermittent, i.e., temporary EMI as interrupted vertical stripes (e.g., mechanically induced interference by the stirrer drive mechanism). Also, any nonuniformity of tuning would be detectable through vertical stripes of nonuniform color (different levels) lengthwise. In the present case, the spikes were found to be present at nearly all secondary tune states except $\ell = 17$, with Fig. 14(b) showing the ASDF for $\ell = 1$. When f is increased, any detectable quasi-periodic variation by EMI in the stir sweep becomes gradually overwhelmed by the increasingly random field variation in the stir process.

Notch filtering of the harmonics in Fig. 12 improves the accuracy of the [0/2]-order Padé approximant and its ASDF, although the first-order approximant prior to any filtering (shown in green in Fig. 15) clearly offers an adequate model and approximation already.

The EMI spikes in Figs. 11(a) and 13(b) are much less prominent than those in Fig. 12(a) and 14(b) because a larger stirrer produces a higher and flatter SDF level. Nevertheless, they appear with the same $\Delta k \simeq 480$. Thus, inefficient stirring detects this EMI more easily. Interestingly, the locations of weak LF local maxima across stir states in Figs. 11(a) and 13(b) correspond with those of local minima for $\nu_{g_E'}(\varpi_k)$ in Fig. 7 across tune states at $f = 2$ GHz. This confirms the common source of EMI affecting both the stirrer and the tuner.

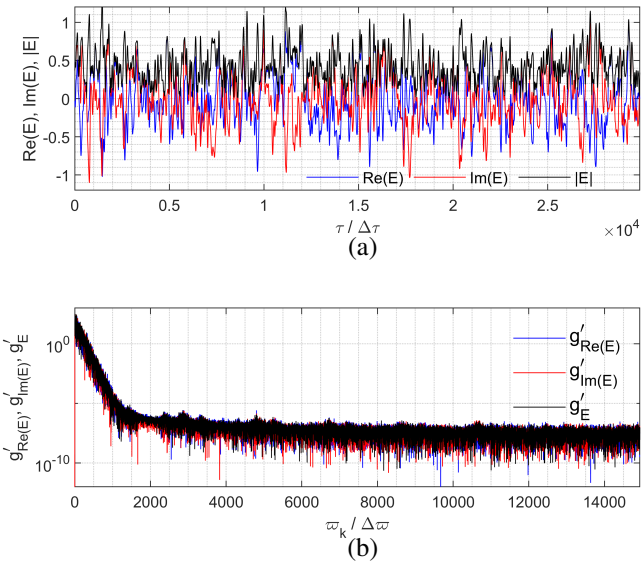

Fig. 13: (a) Stir sweep and (b) associated ASDF of large paddle stirring at $f = 2$ GHz, for an arbitrary tune state of the small paddle ($\ell = 1$).

VII. Conclusion

In this part III, experimental CFs and SDFs were compared with theoretical Padé-based models derived in part I, showing good agreement [1]. Periodogram- and generalized EWK-based methods produce near-identical results (Figs. 1 and 10). First- and second-order Padé approximants for stir ACFs and CCFs were found to outperform Taylor approximations of same and even higher order. Even a simple first-order (one-parameter) Padé model offers accurate ACF values down to

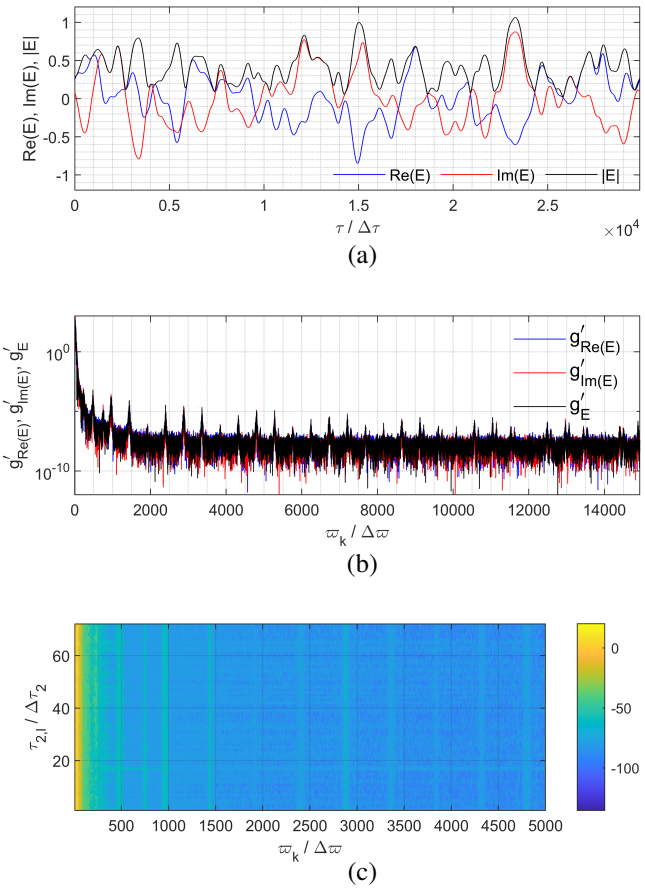

Fig. 14: (a)–(b) Same as Fig. 13 but for interchanged roles of now small paddle stirrer and large paddle tuner; (c) stir spectrogram of g'_E (in dB) as a function of primary stir frequencies $5 \leq \varpi_k/\Delta\varpi \leq 5000$ ($\sim 0.001 \leq \varpi_k \leq 1.052$ rad/s) and secondary tune states $0 \leq \tau_{2,\ell}/\Delta\tau_2 \leq 71$ ($\sim 0 \leq \theta_\ell \leq 355$ deg).

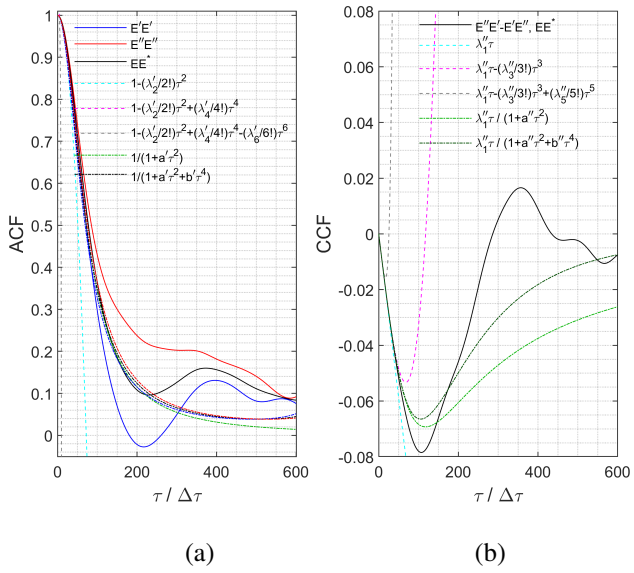

Fig. 15: (a) ACFs and (b) CCFs as in Fig. 4 but for interchanged roles of small and large paddles as stirrer, at $f = 18$ GHz.

$\rho'_E(\tau) \sim 0.1 \ldots 0.3$, with further increasing range of accuracy for increasing efficiency of the stirrer (Figs. 4 and 15).

Extensions to higher-order approximants, offering further improved accuracy or extended domain or range for stir lags or frequencies, are possible by solving cubic or higher-order equations for their roots. However, higher-order expansions rely on higher-order spectral moments $\lambda'^{(\prime)}_m$ as their coefficients. The accurate estimation of $\lambda'^{(\prime)}_m$ from discrete finite-difference stir sweep data or their ACF was found in part II to be prone to rapidly increasing bias and uncertainty with increasing moment order m. This issue is already apparent in the second-order Padé-based model, where some asymptotic spectral features exhibit heightened sensitivity to the spectral kurtosis κ' with ideal zero value (Tbl. I).

Since the DC-to-Nyquist drop of ASDF level is $1/\sqrt{\kappa'}$ for $\kappa' > 0$ [1, eq. (43)], i.e., independent of λ'_2, it offers a pragmatic way of estimating κ' directly from the experimental ASDF itself (Fig. 5), thus bypassing the difficulties in the estimation of individual λ'_m [1, eq. (27)].

The shallower the (negative) slope of the ASDF's envelope, $-\sqrt{2(1-\kappa')/\lambda'_2}$, in going from stir DC to the corner stir frequency ϖ'_c, the higher the stir efficiency. Ideal stirring corresponds to pure white stir noise ($\lambda'_2 \to +\infty$).

The combination of one stirrer and one tuner offers a capability of generating an ensemble of one-dimensional ACFs and SDFs for increased accuracy. It also allows for estimation of the average and the absolute or relative rms spread of the covariance/correlation level for an arbitrary stir lag τ_n, as well as the spectral amplitude of the SDF at a particular normalized stir frequency ϖ_k (Fig. 7). As the number of secondary tune states increases, the ensemble averaged SDF of the stirrer exhibits a reduced spread of amplitude levels across its entire stir band, notably also compared to a concatenation of stir sweeps. The latter's increased number of data points to $N_t \times N_s$ is well known to be unable to reduce spectral spread [6] (Fig. 6). Ensemble averaging of SDFs avoids the need for ad hoc low-pass filtering or Welch's method on a single-trace SDF. This eliminates spectral biasing that is nonuniform across the stir spectrum and which distorts not only the estimated SDF [5], [6] but also SDF-based estimated spectral moments, which is particularly strong near $\varpi_{\max}$.

Finally, at sufficiently low excitation frequencies, the stir SDF enables diagnostics to be performed, e.g., identification of intermittent or permanent sources of EMI (Figs. 11–14), in particular via a stir spectrogram (Fig. 14(c)).

References

[1] L. R. Arnaut, "Correlation and spectral density functions in mode-stirred reverberation – I. Theory," submitted for publication.

[2] L. R. Arnaut and J. M. Ladbury, "Correlation and spectral density functions in mode-stirred reverberation – II. Sampling and noise effects," submitted for publication.

[3] L. R. Arnaut, "Effect of local stir and spatial averaging on the measurement and testing in mode-tuned and mode-stirred reverberation chambers," *IEEE Trans. Electromagn. Compat.*, vol. 43, no. 3, pp. 305–325, Aug. 2001.

[4] L. R. Arnaut, "Threshold level crossings, excursions, and extrema in immunity and fading testing using multistirred reverberation chambers," *IEEE Trans. Electromagn. Compat.,* vol. 62, no. 5, pp. 1638–1650, Oct. 2020.
[5] M. B. Priestley, *Spectral Analysis and Time Series – Vol. 1: Univariate Series.* Academic Press: London, U.K., 1981.
[6] G. M. Jenkins and D. G. Watts, *Spectral Analysis and Its Applications.* Holden-Day: San Francisco, CA, 1968.
[7] F. Moglie and V. Mariani Primiani, "Evaluation of uncorrelation and statistics inside a reverberation chamber in presence of two independent stirrers," *Proc. 2010 IEEE Symp Electromagn. Compat.,* Ft. Lauderdale, FL, pp. 515–519, Jul. 2010.
[8] O. Lundén and M. Bäckström, "Design of experiment. How to improve reverberation chamber mode-stirrer efficiency," FOI Tech. Rep. FOI-R-0468-SE, Linköping, Sweden, Apr. 2002.
[9] L. R. Arnaut, "Effect of size, orientation, and eccentricity of mode stirrers on their performance in reverberation chambers," *IEEE Trans. Electromagn. Compat.,* vol. 48, no. 3, pp. 600–602, Aug. 2006.